Journal of Thermal Analysis and Calorimetry (2024) 149:1725–1744
https://doi.org/10.1007/s10973-024-12885-3

Performing SiO_2-MWCNT/water hybrid nanofluid with differently shaped nanoparticles to enhance first- and second-law features of flow by considering a two-phase approach

Recep Ekiciler[1]

Received: 10 October 2023 / Accepted: 5 January 2024 / Published online: 22 January 2024

Abstract

The utilization of hybrid nanofluids has gained essential consideration in thermal engineering. Changes in the thermal characteristics of the base fluid are responsible for the improved thermal conductivity brought about by hybrid nanoparticles and their shapes. For this goal, in this paper, the two-phase 60%:40% SiO_2-MWCNT/water hybrid nanofluid flow at the Reynolds number range of 3000–10,000 in a square duct is investigated concerning first- and second-law analysis. The turbulent flow regime is modeled using the RNG k–ε turbulence approximation. The hybrid nanofluid is modeled via a mixed model. The parameters used in this study are three different nanoparticle shapes (cylindrical, spherical, and platelet) and nanoparticle volume fractions (0.2%, 0.6%, and 1.0%). The distributions of the Nusselt number, friction factor, entropy generation, exergy destruction, exergy efficiency, temperature, and velocity contours are investigated in detail for the above parameters. It is found that the most significant increases in PEC are seen in hybrid nanofluids with the PC and PP shapes, at 2.27 and 3.24%, respectively. It has been shown that the exergy destruction of hybrid nanofluids with the second nanoparticle forms C and P is 43.90% and 58.74% more than that of a S one when PS-, PC-, and PP-shaped nanoparticles are utilized. The hybrid nanofluid with the PS shape has the highest exergy efficiency, whereas the SP-shaped nanofluid has the lowest.

Keywords Hybrid nanofluid · Two-phase approach · Exergy efficiency · Entropy generation · Passive technique

List of symbols

W	Width of duct (m)
L	Length of the duct (m)
C_p	Specific heat (J kg^{-1} K^{-1})
ρ	Density (kg m^{-3})
q''	Heat flux (W m^{-2})
k	Thermal conductivity (W m^{-1} K^{-1})
μ	Viscosity (Pa s)
Pr	Prandtl number
Re	Reynolds number
ff	Friction factor
T	Temperature (K)
Nu	Nusselt number
h_c	Heat transfer coefficient (W m^{-2} K^{-1})
$\dot{X}_d$	Exergy destruction rate (W)
$(\dot{TEG})'''$	Local thermal entropy generation (W m^{-3} K^{-1})
$(\dot{FEG})'''$	Local frictional entropy generation (W m^{-3} K^{-1})
$(\dot{TTEG})'''$	Total entropy generation per unit volume (W m^{-3} K^{-1})
n	Phase number
φ	Nanoparticle volume fraction

Subscripts

eff	Effective
wa	Wall
w	Water
nf	Nanofluid
m	Mixture
dr	Drift
b	Bulk
o	Outlet

Abbreviations

HybN	Hybrid nanofluid
MWCNT	Multi-walled carbon nanotube
NPVF	Nanoparticle volume fraction
TEG	Thermal entropy generation
FEG	Frictional entropy generation

✉ Recep Ekiciler
recepekiciler@gazi.edu.tr

[1] Mechanical Engineering Department, Engineering Faculty, Gazi University, 06570 Ankara, Turkey

TTEG	Total entropy generation
P	Platelet shape
C	Cylindrical shape
S	Spherical shape
SS	Hybrid nanofluid with first and second shapes of nanoparticles S
SC	Hybrid nanofluid with first and second shapes of nanoparticles S and C, respectively
SP	Hybrid nanofluid with first and second shapes of nanoparticles S and P, respectively
CC	Hybrid nanofluid with first and second shapes of nanoparticles C
CS	Hybrid nanofluid with first and second shapes of nanoparticles C and S, respectively
CP	Hybrid nanofluid with first and second shapes of nanoparticles C and P, respectively
PP	Hybrid nanofluid with first and second shapes of nanoparticles P
PC	Hybrid nanofluid with first and second shapes of nanoparticles P and C, respectively
PS	Hybrid nanofluid with first and second shapes of nanoparticles P and S, respectively

Introduction

Techniques that enhance heat transmission are often used in a broad range of applications, such as air conditioning, chemical reactors, refrigeration, and heat recovery [1–4]. Forced convection is one of the best approaches to moving heat from one place to another. It works because an outside force, such as a fan, pump, suction device, etc., moves the fluid. This method is often utilized in very complicated systems, like nuclear power [5], cooling solar cells [6], cooling electrical circuits [7], etc.

In engineering technology, ducts are widely employed for various purposes, such as heat exchangers, electrical boards, etc. With the growing need for energy, thermal devices are now looking for ways to transfer heat more quickly. Active and passive strategies are used to achieve the desired improvement in heat transfer. Active techniques need an additional power source, whereas passive methods alter the thermal properties of the flow or the system's design. Using highly conductive materials, such as nanoparticles or porous materials, is an example of passive methods. One of these techniques is the increasing adoption of nanofluids, thermal devices, in ducts. Several applications, including better oil recovery, lubrication, heat transfer, and drug administration, benefit from the use of nanofluids, which are suspensions of nanoparticles (at least one dimension lower than 100 nm) in a base fluid with superior wettability, rheological, and thermal features [8–10]. The thermal conductivity of Cu-water and Fe_3O_4/kerosene nanofluid was found to be increased by 78% by Xuan and Li [11] and by 34% by Yu et al. [12], respectively. Using a microchannel heat sink, Lau et al. [13] analyzed how various nanofluids behave. A drop of 7 K was obtained when 5% nanoparticles of Al_2O_3 were dispersed to the base fluid. Davarnejat and Jamshidzaded [14] investigated the heat transfer characteristics of a water-MgO subjected to turbulent flow conditions and a temperature that was held constant along the wall. The variables employed in the design process were Reynolds numbers (Res) between 3000 and 19,000 and water–MgO nanofluid concentrations. According to the findings, the Nusselt number (Nu) and the performance of the two-phase models improved with increasing nanoparticle concentration and Re. TiO_2-water nanofluid was investigated by Subramanian et al. [15] for laminar, transitional, and turbulent flows in a heat exchanger having a double-pipe counter-flow. By helping nanofluids, they could make a 15% rise in heat transfer coefficient over the water. Using the turbulence model, Mahato et al. [16] studied numerically the fluid flow and heat transfer of water/Al_2O_3 and water/CuO nanofluids with a volume percentage of nanoparticles between 1 and 3% in a clockwise–counterclockwise twisted square duct. They found that at 1% of Al_2O_3 nanoparticles, the mean percentage rise in Nu is roughly 0.1–0.5% greater than the findings obtained using plain duct with base water, while an increment of 0.5–1% is found for 1% of CuO. Forced convective heat transport of a Cu-water nanofluid was investigated numerically by Heidary and Kermani [17] in sinusoidal ducts. They discovered that combining the nanofluid with the horizontal waves in the walls may boost heat transmission by a factor of 1.5. Liu et al. [18] numerically investigated nanoparticle morphologies' effect on heat transfer in a curved duct. The water–Al_2O_3 nanofluid was utilized as a working fluid in their experiments. The findings demonstrated that the platelet nanoparticle form produces the most remarkable rise in pressure loss and convective heat transfer coefficient. Convection heat transfer of a water/Al_2O_3 nanofluid was experimentally examined by Heris et al. [19] in a square cross-sectioned duct in laminar flow. At a volume fraction of 2.5%, nanoparticles were shown to improve heat transmission by up to 27.6% compared to water. Outcomes also showed a rise in the convective heat transfer coefficient when the volume percentage of nanoparticles in the sample increased.

Nowadays, hybrid nanofluids (HybNs) enhance heat transfer in many engineering applications. A HybN is an advanced form of heat transfer fluid that consists of two or more nanoparticles. To learn more about the cooling capabilities of different alumina HybNs, Bhattad et al. [20] performed a sequence of studies. In their experimentations adopting water as the base fluid, Al_2O_3-MWCNT (4:1) was shown to have the most significant increase in the coefficient of heat transfer by roughly 31.2%. Tests of CuO-Al_2O_3- and CuO-SiO_2 HybNs and water were conducted in a pulsing

heat pipe, and their results were classed experimentally and numerically by Zufar et al. [21]. The CuO-SiO_2 HybN was said to have more excellent performance and a maximum drop of nearly 55% in the thermal resistance of the heat pipe compared to water. A more significant irreversibility decrease was shown for double counter-twisted tape insertion, as determined by the analysis of GNP HybN by Bahiraei et al. [22].

From the preceding summary, it is clear that research into the properties of fluid flows, whether they include nanofluids or more traditional fluids for heat transfer, is an essential area of inquiry. Furthermore, given the growing fascination with hybrid nanofluid, it is vital to investigate the impact of the nanoparticle's shape on the device's efficiency. Therefore, the goal of this study is to search the influence of the 60%:40% SiO_2-MWCNT/water HybN with different forms of nanoparticles (platelet (*P*), cylindrical (*C*), and spherical (*S*)) on the square duct's heat transfer. The addition of the second-law analysis further strengthens the research. This research shed light on developing and implementing thermofluid-flow devices over multiphysical issues. This work's methodology and findings from system analyses may be applied to heat exchangers and other comparable thermal systems and devices. The structure of the study is also presented in Fig. 1.

Numerical method

Physical model

Figure 2 shows a schematic depiction of the square duct. Throughout a square duct with $W = 10$ mm and $L = 1000$ mm, a HybN with constant input velocities and temperatures moves. Constant heat flux ($q'' = 29$ kW m^{-2}) is exposed to all the duct walls. A 60%:40% SiO_2-MWCNT/water HybN is selected as a working fluid. The thermophysical properties of the SiO_2 and MWCNT nanoparticles and water are given in Table 1.

Governing equations

Analyzing nanofluid flows uses single-phase and two-phase models. The nanosized supplements and primary fluid have similar temperatures and speeds in the single-phase

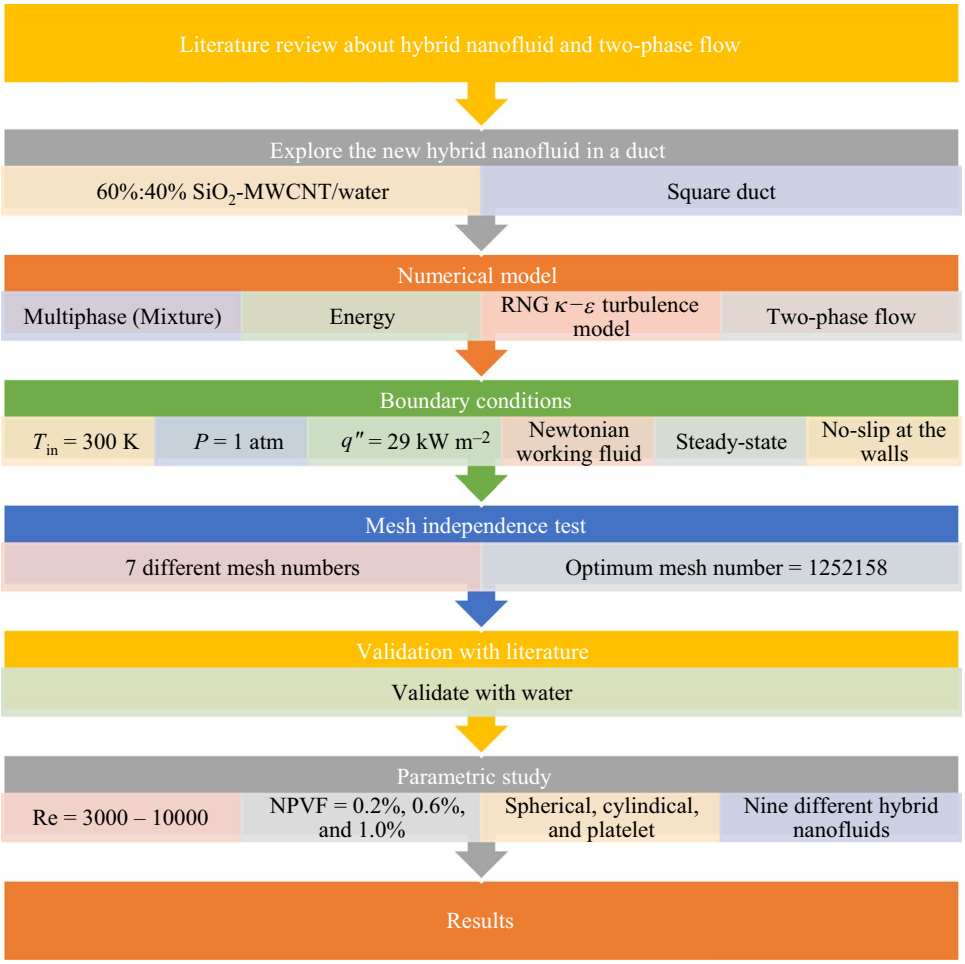

Fig. 1 Methodology of the study

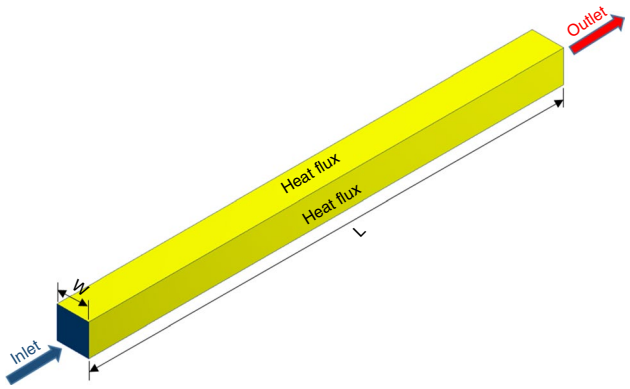

Fig. 2 Physical model of the study

Table 1 Thermophysical properties of nanoparticles and water

	ρ/kg m^{-3}	C_p/J kg^{-1} K^{-1}	k/W m^{-1} K^{-1}	μ/Pa s
SiO_2 [23]	2200	740	1.38	–
MWCNT [24]	1600	796	3000	–
Water [25]	998.2	4182	0.6	0.001003

technique. In this sense, the nanofluid might be considered a homogeneous entity. This simple, low-cost method has been employed in several nanofluid experiments. The Eulerian–Eulerian and mixture models are two-phase techniques. The nanosized supplements' speed and the leading fluid's temperature are dissimilar in a two-phase combination. In this system, the formulas determining the nanosized supplements' volume fraction are additionally calculated. With the help of the Eulerian–Eulerian model, the core fluid and the nanosized supplements have been treated like two distinct phases. There is a focus on independently adapting the equations of energy, momentum, and continuity to every stage, and interactions of phase are additionally investigated. For the method, fluids and nanosized supplements may have varied temperatures and velocities. Due to its complexity and high computational cost, the Eulerian–Eulerian model is seldom used to research nanofluid flow. The two-phase mixing approach has more complicated interactions and lower processing costs than the Eulerian–Eulerian and single-phase models. The two-phase mixed technique is more accurate than the Eulerian–Eulerian and single-phase models; hence, it was utilized in this study. Evaluation of the flow pattern and convective heat transport of the HybNs under turbulent flow conditions is achieved by solving the equations for the conversion of volume fraction, mass, momentum, and energy using the two-phase mixture technique. The equations are given below [26]:

Conservation of volume fraction:

$$\nabla.\left(\varphi_p\rho_p\vec{V}_m\right) = -\nabla.\left(\varphi_p\rho_p\vec{V}_{dr,p}\right) \tag{1}$$

where φ_i stands for the volume fraction of the ith phase ($1 \le i \le n$), and n refers to the total phase numbers. The two phases in this research are denoted by the superscripts p and s, which stand for "primary" (the liquid phase or base fluid) and "secondary" (the solid phase or the nanoparticle), respectively. The m in front of the symbol indicates that the mixture has specific characteristics. Mass, momentum, and energy conservation equations are written down explicitly [26].

Conservation of mass:

$$\nabla.\left(\varphi_m\vec{V}_m\right) = 0 \tag{2}$$

Conservation of momentum:

$$\nabla.\left(\rho_m\vec{V}_m\vec{V}_m\right) = -\nabla P + \nabla.\left(\mu_m\left(\nabla\vec{V}_m + \nabla\vec{V}_m^T\right)\right) + \nabla.\left(\sum_{i=1}^{n}\left(\varphi_i\rho_i\vec{V}_{dr,i}\vec{V}_{dr,i}\right)\right) \tag{3}$$

Conservation of energy:

$$\nabla\cdot\sum_{i=1}^{2}\left(\varphi_i\vec{V}_i\left(\rho_i h_i + P\right)\right) = \nabla.\left(k_{eff}\nabla T\right) \tag{4}$$

where P, h, and k_{eff} are average pressure, sensible enthalpy, and effective thermal conductivity, respectively.

$$k_{eff} = \sum\varphi\left(k_i + k_t\right) \tag{5}$$

where k_t is turbulent thermal conductivity.

$$\vec{V}_m = \frac{\sum_{i=1}^{n}\left(\varphi_i\rho_i\vec{V}_i\right)}{\rho_m} \tag{6}$$

where $\vec{V}_m$ is the mean velocity.

$$\vec{V}_{dr,i} = \vec{V}_i - \vec{V}_m \tag{7}$$

where $\vec{V}_{dr,i}$ is the drift velocity for the secondary phase (i).

$$\vec{V}_{sp} = \vec{V}_s - \vec{V}_p \tag{8}$$

where $\vec{V}_{sp}$ is the drift velocity. Also, the slip velocity may be obtained from the following equation [27]:

$$\vec{V}_{sp} = \frac{d_s^2\left(\rho_s - \rho_m\right)\vec{a}}{18\mu_p f_{drag}} \tag{9}$$

where d_s is the nanoparticle's nominal diameter.

The correlation is given to obtain the drag function [28]:

$$f_{\text{drag}} = \begin{cases} 1 + 0.15\text{Re}_s^{0.687}, & \text{Re}_s \le 1000 \\ 0.0183\text{Re}_s, & \text{Re}_s \ge 1000 \end{cases} \tag{10}$$

where Re_s represents the nanoparticles' Re.

$$\vec{a} = -\left(\vec{V}_m \cdot \nabla\right) \cdot \vec{V}_m \tag{11}$$

where $\vec{a}$ denotes acceleration.

The effective specific heat ($C_{p,m}$) is as follows:

$$C_{p,m} = \sum_{i=1}^{n} (C_{p,i}\varphi_i) \tag{12}$$

The effective thermal conductivity (k_m):

$$k_m = \sum_{i=1}^{n} (k_i\varphi_i) \tag{13}$$

The effective viscosity (μ_m):

$$\mu_m = \sum_{i=1}^{n} (\mu_i\varphi_i) \tag{14}$$

The effective density (ρ_m):

$$\rho_m = \sum_{i=1}^{n} (\rho_i\varphi_i) \tag{15}$$

The RNG k–ε model is selected for the numerical calculation since it gives more accurate results [29]. k (turbulent kinetic energy) and ε (dissipation) are obtained with the RNG k–ε model and are presented below, respectively [30]:

$$\begin{aligned} &\frac{\partial\left(\rho k\bar{u}\right)}{\partial x} + \frac{\partial\left(\rho k\bar{v}\right)}{\partial y} - \frac{\partial}{\partial x}\left[\left(\mu + \frac{\mu_t}{\sigma_k}\right)\frac{\partial k}{\partial x}\right] \\ &+ \frac{\partial}{\partial y}\left[\left(\mu + \frac{\mu_t}{\sigma_k}\right)\frac{\partial k}{\partial y}\right] + G_k + G_b - \rho\varepsilon - D \end{aligned} \tag{16}$$

$$\begin{aligned} &\frac{\partial\left(\rho\varepsilon\bar{u}\right)}{\partial x} + \frac{\partial\left(\rho\varepsilon\bar{v}\right)}{\partial y} - \frac{\partial}{\partial x}\left[\left(\mu + \frac{\mu_t}{\sigma_\varepsilon}\right)\frac{\partial \varepsilon}{\partial x}\right] \\ &+ \frac{\partial}{\partial y}\left[\left(\mu + \frac{\mu_t}{\sigma_\varepsilon}\right)\frac{\partial \varepsilon}{\partial y}\right] \\ &+ C_{\varepsilon 1} f_1 \frac{\varepsilon}{k}\left(G_k + C_{\varepsilon 3} G_b\right) - C_{\varepsilon 2} f_2 \frac{\varepsilon^2}{k} + E \end{aligned} \tag{17}$$

the constants $C_{\varepsilon 1}, C_{\varepsilon 2}, C_{\varepsilon 3}$, f_1, and f_2 are 1.42, 1.68, 1.0, 1.0, and 1.0, respectively. The $\sigma_k = 1.39$ and $\sigma_\varepsilon = 1.39$ define the inverse turbulent Prandtl numbers for k and ε, respectively. The constants $D = 2\nu\left(\frac{\partial k^{1/2}}{\partial y}\right)$ and $E = 2\mu\mu_t\left(\frac{\partial^2 u}{\partial y^2}\right)^2$. By solving Eq. (18), we can calculate the G_k, which characterizes the rate of creation of turbulent kinetic energy owing to the average velocity gradients:

$$G_k = \mu_t\left(\frac{\partial u_i}{\partial x_j} + \frac{\partial u_j}{\partial x_i}\right)\frac{\partial u_i}{\partial x_j} - \frac{2}{3}\rho k\delta_{ij}\frac{\partial u_i}{\partial x_j} \tag{18}$$

An increase in turbulent kinetic energy, denoted by G_b, is produced by buoyancy since the investigated flow field is isothermal, $G_b = 0$.

Boundary conditions

The heat flux throughout all walls, which is 29 kW m^{-2}, is used as one of the boundary conditions in the solution of the preceding formulas. It is presumed that a uniform inlet velocity for the nanofluid and a temperature of 300 K. It is assumed that there will be no slip along the interior walls and that atmospheric pressure is taken into account at the pressure outlets.

Data reduction

The system of interest here is a HybN consisting of nanoparticles (SiO_2 and MWCNT) of varying shapes flowing through a square duct in three dimensions. Nanoparticles of SiO_2 offer several benefits, including outstanding toughness and rigidity, appealing physical features, and exceptional thermal stability [31]. Recently, the remarkable thermal conductivity of MWCNT has garnered attention [32]. To make the outcomes of the research more accessible, the author performed numerical analyses and then translated the results into a mathematical language that can be understood by the general public using the following equation.

Below is a description of the typical convective heat transfer coefficient [33].

$$h_c = \frac{q''}{\left(T_{wa} - T_b\right)} \tag{19}$$

where q'' (W m^{-2}), T_{wa} (K), and T_b (K) denote heat flux, wall temperature, and bulk temperature, respectively. The T_b is calculated from the following equation:

$$T_b = \frac{T_i + T_o}{2} \tag{20}$$

where T_i (K) and T_o (K) represent inlet and outlet temperature, respectively.

The average Nu is obtained from the equation given below:

$$\text{Nu} = \frac{h_c D_h}{k} \tag{21}$$

where D_h (m) and k (W m^{-1} K^{-1}) are the working fluid's hydraulic diameter and thermal conductivity.

The friction factor can be obtained from the equation given below:

$$ff = \frac{\Delta P}{\left(\frac{L}{D_h}\right)\left(\frac{\rho V^2}{2}\right)} \tag{22}$$

where ΔP (Pa), L(m), ρ (kg m^{-3}), and V (m s^{-1}) denote pressure drop, length of the duct, the density of the working fluid, and velocity of the working fluid, respectively.

Several formulae have been provided below to compute the physical characteristics of HybNs, including their density, thermal conductivity, specific heat, and dynamic viscosity.

The thermophysical parameters of the HybN, such as density and specific heat, vary with the NPVFs. The mixing model may be used to calculate the density and specific heat of the HybN [34].

The density of the HybN:

$$\rho_{HybN} = \rho_{SiO_2}\varphi_{SiO_2} + \rho_{MWCNT}\varphi_{MWCNT} + \left(1 - \varphi_{SiO_2} - \varphi_{MWCNT}\right)\rho_w \tag{23}$$

The specific heat of the HybN:

$$\left(C_p\right)_{HybN} = \frac{\rho_{SiO_2}C_{p,SiO_2}\varphi_{SiO_2} + \rho_{MWCNT}C_{p,MWCNT}\varphi_{MWCNT} + \left(1 - \varphi_{SiO_2} - \varphi_{MWCNT}\right)\rho_w C_{p,W}}{\rho_{HybN}} \tag{24}$$

The thermophysical characteristics (viscosity and thermal conductivity) of the HybN rely on particle shape and NPVF. This theoretical study considers nanoparticle concentration and shape. The thermal conductivity can be calculated by the Maxwell equation [35]:

$$\frac{k_{nf}}{k_w} = \frac{k_{SiO_2 \text{ or } MWCNT} + (n-1)k_w + (n-1)\varphi\left(k_{SiO_2 \text{ or } MWCNT} - k_w\right)}{k_{SiO_2 \text{ or } MWCNT} + (n-1)k_w - \left(k_{SiO_2 \text{ or } MWCNT} - k_w\right)} \tag{25}$$

where n represents the shape factor. n can be calculated by the following equation:

$$n = \frac{3}{\Psi} \tag{26}$$

where Ψ is defined as sphericity.

For P-shaped: $n = 5.7$ and $\Psi = 0.52$.

For C-shaped: $n = 4.9$ and $\Psi = 0.61$.

For S-shaped:$n = 3$ and $\Psi = 1$.

It may be written down the effective thermal conductivity of a HybN built on P-, C-, and S-shaped nanoparticles like this, respectively:

$$\frac{k_{nf}}{k_w} = \frac{k_{SiO_2 \text{ or } MWCNT} + 4.7k_w + 4.7\varphi\left(k_{SiO_2 \text{ or } MWCNT} - k_w\right)}{k_{SiO_2 \text{ or } MWCNT} + 4.7k_w - \left(k_{SiO_2 \text{ or } MWCNT} - k_w\right)} \tag{27}$$

$$\frac{k_{nf}}{k_w} = \frac{k_{SiO_2 \text{ or } MWCNT} + 3.9k_w + 3.9\varphi\left(k_{SiO_2 \text{ or } MWCNT} - k_w\right)}{k_{SiO_2 \text{ or } MWCNT} + 3.9k_w - \left(k_{SiO_2 \text{ or } MWCNT} - k_w\right)} \tag{28}$$

$$\frac{k_{nf}}{k_w} = \frac{k_{SiO_2 \text{ or } MWCNT} + 2k_w + 2\varphi\left(k_{SiO_2 \text{ or } MWCNT} - k_w\right)}{k_{SiO_2 \text{ or } MWCNT} + 2k_w - \left(k_{SiO_2 \text{ or } MWCNT} - k_w\right)} \tag{29}$$

For the various nanoparticle shapes, the viscosity can be defined as [34]:

For P-shaped:

$$\mu_{nf} = \mu_w\left(1 + 37.1\varphi + 612.6\varphi^2\right) \tag{30}$$

For C-shaped:

$$\mu_{nf} = \mu_w\left(1 + 13.5\varphi + 904.4\varphi^2\right) \tag{31}$$

For S-shaped:

$$\mu_{nf} = \mu_w\left(1 + 2.5\varphi + \varphi^2\right) \tag{32}$$

The interpolation approach, related to the NPVF and shape of the nanoparticles, may be utilized to assess the effective thermal conductivity and viscosity characteristics of various HybN compositions.

$$k_{HybN} = \frac{k_{SiO_2}\varphi_{SiO_2} + k_{MWCNT}\varphi_{MWCNT}}{\varphi} \tag{33}$$

$$\mu_{HybN} = \frac{\mu_{SiO_2}\varphi_{SiO_2} + \mu_{MWCNT}\varphi_{MWCNT}}{\varphi} \tag{34}$$

where $\varphi = \varphi_{SiO_2} + \varphi_{MWCNT}$.

Re is obtained from the following equation [36]:

$$\mathrm{Re} = \frac{\rho V D_h}{\mu} \tag{35}$$

The performance evaluation criterion (PEC) is obtained from the following equation [36]:

$$\mathrm{PEC} = \frac{\left(\mathrm{Nu}_{HybN}/\mathrm{Nu}_w\right)}{\left(ff_{HybN}/ff_w\right)^{1/3}} \tag{36}$$

The second law of thermodynamics provides a new window through which to analyze thermofluidic devices: the quantity of wasted useful energy. The overall energy value lost in an operation is heavily influenced by thermal and frictional irreversibilities. The second-law analysis measures the production of entropy, the destruction of exergy, and the effectiveness of the second law.

The thermal entropy generation (TEG) rate may be locally obtained by helping the following equation [37]:

$$(\dot{\mathrm{TEG}})''' = \frac{k_{\mathrm{m}}}{T}\left\{\left(\frac{\partial T}{\partial x}\right)^2 + \left(\frac{\partial T}{\partial y}\right)^2 + \left(\frac{\partial T}{\partial z}\right)^2\right\} \tag{37}$$

The frictional entropy generation (FEG) rate may be locally obtained by helping the following equation [37]:

$$(\dot{\mathrm{FEG}})''' = \frac{\mu_{\mathrm{m}}}{T}\left\{2\left[\left(\frac{\partial u}{\partial x}\right)^2 + \left(\frac{\partial v}{\partial y}\right)^2 + \left(\frac{\partial w}{\partial z}\right)^2\right] + \left(\frac{\partial u}{\partial y} + \frac{\partial v}{\partial x}\right)^2 + \left(\frac{\partial u}{\partial z} + \frac{\partial w}{\partial x}\right)^2 + \left(\frac{\partial w}{\partial y} + \frac{\partial v}{\partial z}\right)^2\right\} \tag{38}$$

where u, v, and w represent the velocity in the x, y, and z directions.

The total entropy generation (TTEG) rate per unit volume is defined as the following equation [37]:

$$(\dot{\mathrm{TTEG}})''' = (\dot{\mathrm{TEG}})''' + (\dot{\mathrm{FEG}})''' \tag{39}$$

The global values of the entropy generation are derived from integrating these local values throughout the whole volume.

$$(\dot{\mathrm{TEG}})''' = \int (\dot{\mathrm{TEG}})''' \, \mathrm{d}V \tag{40}$$

$$(\dot{\mathrm{FEG}})''' = \int (\dot{\mathrm{FEG}})''' \, \mathrm{d}V \tag{41}$$

$$(\dot{\mathrm{TTEG}})''' = \int (\dot{\mathrm{TTEG}})''' \, \mathrm{d}V \tag{42}$$

The exergy destruction theory is a valuable technique that may be used to determine the extent of the beneficial work lost throughout a procedure. The following equation is used in this investigation to determine the amount of exergy that the working fluid has lost [38]:

$$\dot{X}_{\mathrm{d}} = (\dot{\mathrm{TTEG}})T_0 \tag{43}$$

where T_0 (K) is the ambient temperature.

The sole incoming exergy to the process, specified by the given formula [38], is the exergy transmitted from the duct wall to the working fluid.

$$\dot{X}_{\mathrm{in}} = q''A\left(\frac{T_{\mathrm{HybN}}}{T_{\mathrm{w}}}\right) \tag{44}$$

The second law of efficiency can be obtained by the equation below [38]:

$$\eta_{\mathrm{II}} = \frac{\dot{X}_{\mathrm{in}} - \dot{X}_{\mathrm{d}}}{\dot{X}_{\mathrm{in}}} = 1 - \frac{\dot{X}_{\mathrm{d}}}{\dot{X}_{\mathrm{in}}} \tag{45}$$

Numerical calculation and validity of the study

As mentioned in the preceding section, the governing equations have been solved using the finite volume technique with the help of a commercial CFD simulator called ANSYS Fluent. Using a two-phase mixed model, SiO_2-MWCNT/water HybNs with different shapes of nanoparticles are simulated under turbulent flow using the RNG k–ε turbulence model. In the numerical calculation, y^+ is approximately equal to unity. For the momentum and energy equations, the second-order upwind technique is used, and the SIMPLE algorithm is used to connect the velocity and pressure components. The convergence requirements for the preceding equations are 10^{-6} to get a precise solution.

This research aimed to assure reliable outcomes and provide reproducible grid-size results by testing various grid-size systems. The developments regarding grid independency are given for water at Re of 10,000 in Table 2. The optimum mesh number is selected as 1,252,158. Also, the mesh distribution of the duct is presented in Fig. 3.

A comparison shows the Nu of the water and the correlation of Dittus–Boelter [39] ($\mathrm{Nu} = 0.023\mathrm{Re}^{0.8}\mathrm{Pr}^{0.4}$) in Fig. 4. The maximum deviation of Nu between this study and Dittus–Boelter is 4.1%. Furthermore, the comparison of the numerical ff values between the Petuhhov and Blasius correlations is presented in Fig. 5. The highest error of ff about 12% and 10% for Petukhov ($\mathrm{ff} = (0.790\ln\mathrm{Re} - 1.64)^{-2}$ [40]) and Blasius ($\mathrm{ff} = 0.316\mathrm{Re}^{-0.25}$ [41]) correlations, respectively. Using the comparisons given below, it can be seen that the current simulations are accurate and reliable.

Table 2 Mesh independence test

Mesh number	Nu	ff	Deviation of Nu/%	Deviation of ff/%
20367	92.256	0.035146	–	–
62352	87.214	0.031547	5.78118	11.4084
188328	81.543	0.030266	6.95461	4.23247
534366	79.964	0.029941	1.97464	1.08547
881262	79.175	0.029468	0.99653	1.60513
1252158	78.833	0.029215	0.43383	0.86599
1628141	78.624	0.029208	0.26582	0.02397

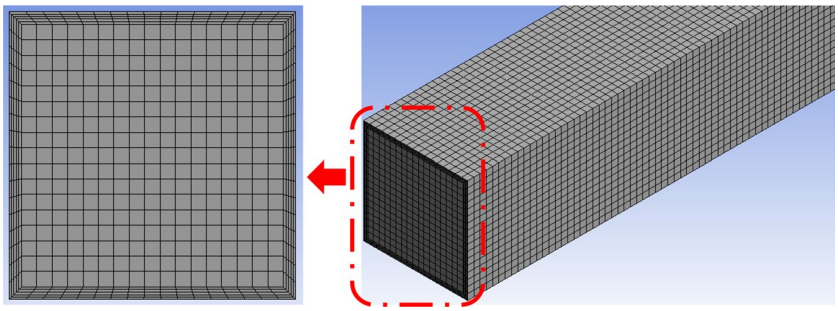

Fig. 3 Mesh distribution of the duct

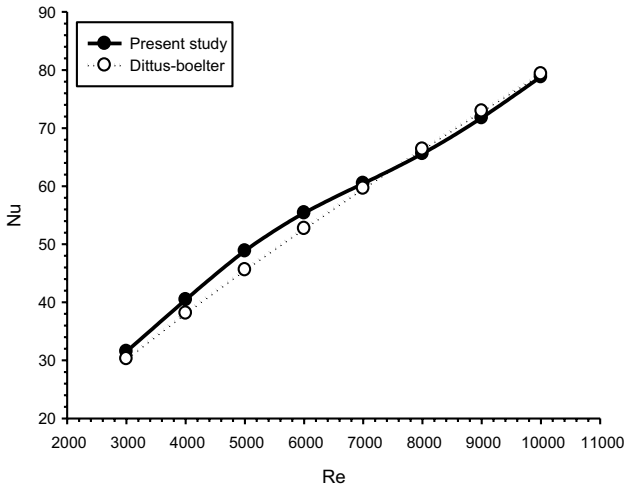

Fig. 4 Validation of Nu

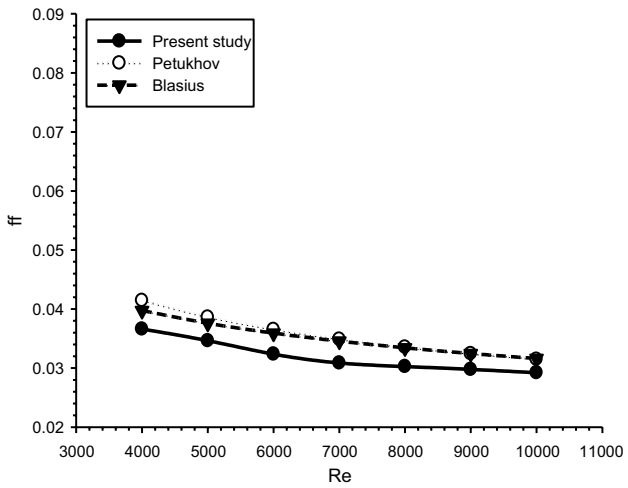

Fig. 5 Validation of ff

Results and discussion

In this part, the numerical outcomes of the current simulations are reported. The effects of NPVFs and shapes of nanoparticles on heat transfer and flow features concerning first- and second-law analysis are investigated for different Res in detail.

Effects of nanoparticle shape and NPVF

Figure 6 shows the variation of the Nu of the 60%:40% SiO_2-MWCNT/water HybN with different nanoparticle volume fractions (NPVFs) and different nanoparticle shapes at a constant Re of 1000. Looking at the graph, the Nu tends to increase in NPVFs in other nanoparticle shapes, except for using *SS*. The decrease in Nu in *SS* shows that the heat conduction coefficient rises more than the heat transfer

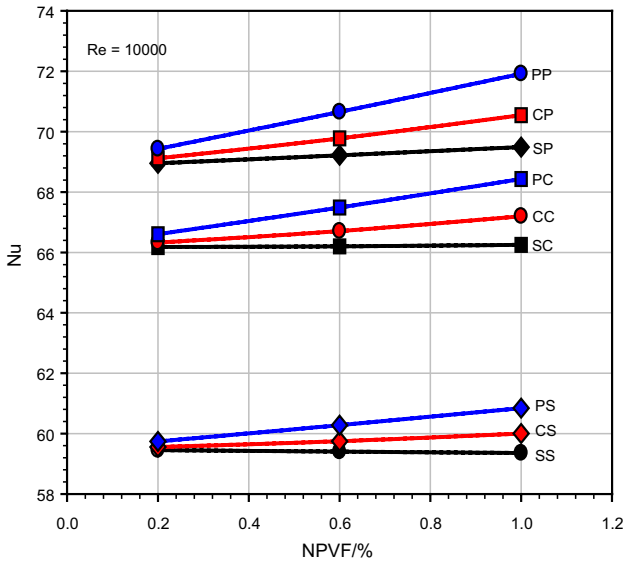

Fig. 6 Variations of Nu for different forms of nanoparticles and NPVF

coefficient. This reduction is calculated as 0.16%. In other words, increasing the NPVF from 0.2 to 1.0% when using *SS* does not affect the Nu. Particularly in the case that the first nanoparticle shape is *S*, the variation of the Nu with the NPVFs increases less than the use of other nanoparticle shapes. The Nu of the HybN formed by the *S* as the first nanoparticle shape is obtained in the *second shape's S, C, and P nanoparticle shapes* in increasing order. *As the first nanoparticles, C and P* do not change the ascending order. With the second nanoparticle shape being *S*, the Nu is highest in *P* and lowest in *S*. In addition, if the second nanoparticle shape is *C* and *P*, the nanoparticle shape with the highest and lowest Nu is *P* and *S*, respectively. As can be seen from the graph, the effect on the change of the Nu by changing the nanoparticle shape is much higher than changing the NPVF. For example, at 1.0% NPVF, the Nu shows a 19.85% increase in *PP* compared to *CS* when *CS* and *PP* nanoparticle shapes are compared. However, when the NPVF increases from 0.2 to 1.0%, the rise in Nu in *CS* and *PP* is 0.75% and 3.57%, respectively.

In Fig. 7, the effects of the 60%:40% SiO_2-MWCNT/water HybN with different nanoparticle shapes (SS, SC, SP, CS, CC, CP, PS, PC, and PP) and different NPVFs (0.2%, 0.6%, and 1.0%) are shown on the variation of pressure drop at constant Re. As the NPVF increases, the pressure drop in all nanoparticle shapes increases. As the HybN's viscosity increases with the increase in the NPVF, the boundary layer thickness also increases. In addition, the fluid velocity increases with the rise in the NPVF. Shear stress on nanoparticles also increases with the increase in velocity. As a result, the pressure loss also increases. Looking at the graph, the HybN with the first nanoparticle shape *P* has the highest pressure drops, while the HybN with the first nanoparticle shape *S* has the lowest pressure drops. While the pressure drop of the HybN with the first nanoparticle shape *S* increases linearly, the pressure drop change parabolically increases faster in the first nanoparticle shapes *C* and *P*. Also, changing the nanoparticle shape has a greater influence on the pressure loss than changing the NPVF. In 1.0% HybNs with the same nanoparticle shape, PP and CC increase the pressure drop by about 47% and 10% compared to *SS*.

Figure 8 depicts the variation in ff at a constant Re for a 60%:40% SiO_2-MWCNT/water HybN with various nanoparticle shapes and NPVFs (0.2%, 0.6%, 1.0%). Looking at the graph, increases and decreases are seen in the ff depending on the nanoparticle shape. It has been determined that as the NPVF increases, HybNs other than *SP*- and *CS*-shaped HybNs increase the ff. Since *SP*- and *CS*-shaped HybNs have a higher velocity value than other nanofluids, the ff decreases. With the increase of the NPVF, the highest ff increase is 2.15% in the HybN formed with *CC*, while the HybN created with *SP* shows the highest decrease in ff with 1.92%. When the NPVF is 1.0%, the *PP*-shaped HybN increases the ff by 5.54% compared to the *SP*-shaped HybN. This indicates that the nanoparticle shape is more dominant than the NPVF on the ff. When *SP*, *SS*, and *SC*, which have the same first nanoparticle shape, are compared, when the NPVF is 0.2%, *SP* has the highest ff, while with the increase in NPVF, it has the lowest ff. This situation can be explained as the percentage increase in velocity increasing more than the pressure loss. Comparing *CS*, *CC,* and *CP*, *CS* is approximately 1.0% larger than *CC* and 1.75% smaller than *CP* at an NPVF of 0.2%.

Figure 9 shows that the PEC changes at a constant Re of 10,000 for a 60%:40% SiO_2-MWCNT/water HybN with various nanoparticle shapes and NPVFs. Considering the NPVF of 0.2%, the PEC numbers in descending order are *PP*, *SP*, *CP*, *PC*, *SC*, *CC*, *CS*, *SS*, and *PS*. However, when the NPVF is 0.6% and 1.0%, the order is changed to *PP*, *SP*, *CP*, *PC*, *CC*, *SC*, *PS*, *CS*, and *SS*. When the NPVF is

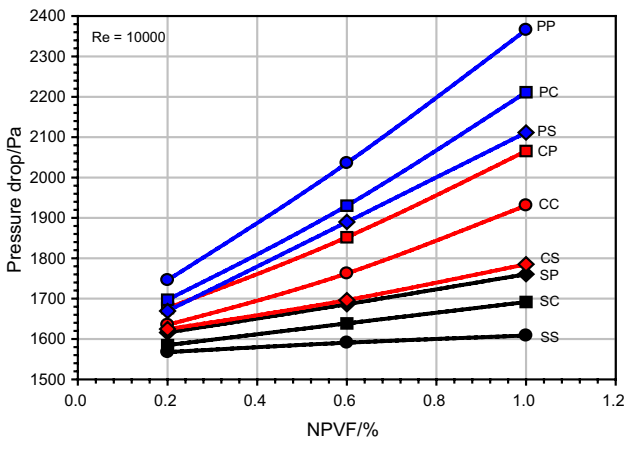

Fig. 7 Distributions of pressure drop for different shapes of nanoparticles and NPVF

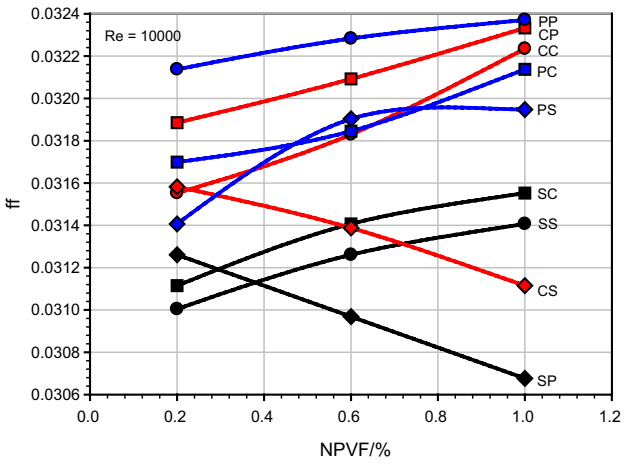

Fig. 8 Distributions of ff for different shapes of nanoparticles and NPVF

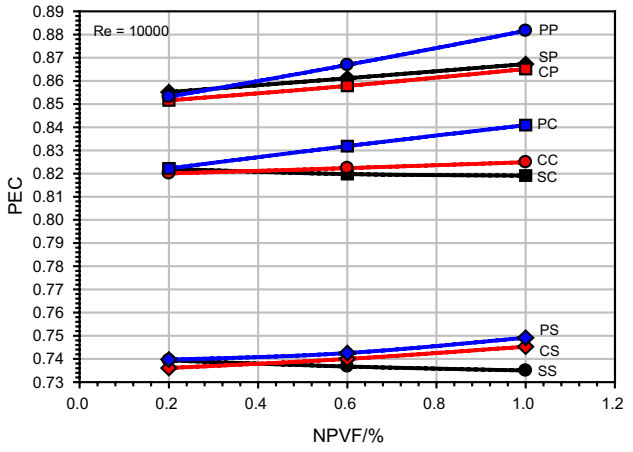

Fig. 9 Variations of PEC for different shapes of nanoparticles and NPVF

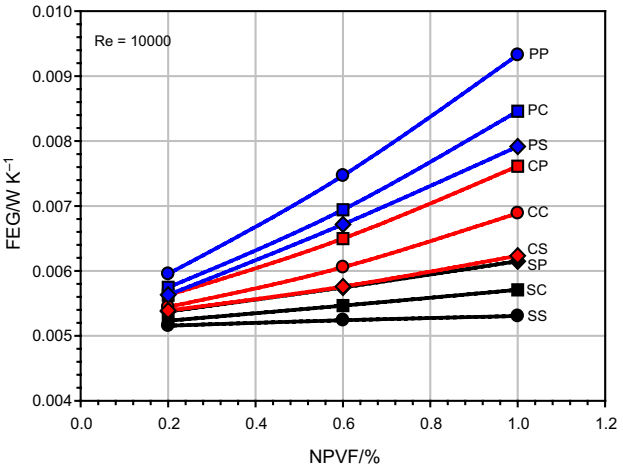

Fig. 11 Variations of FEG for different shapes of nanoparticles and NPVF

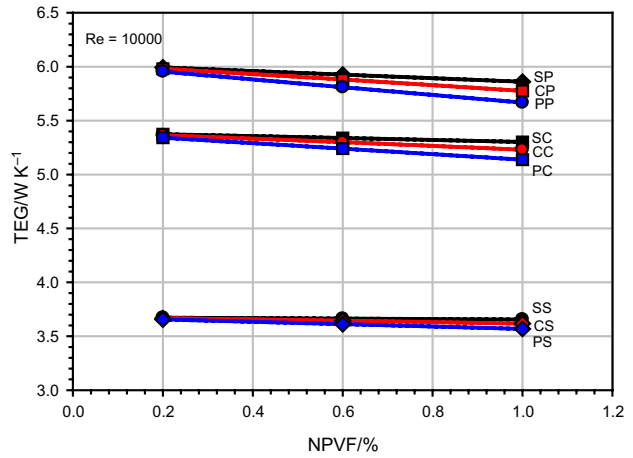

Fig. 10 Distributions of TEG for different shapes of nanoparticles and NPVF

increased from 0.2 to 1.0%, the PEC number decreases by 0.5% and 0.35% in SS- and SC-shaped HybNs, respectively. This can be explained as the rate of increase in heat transfer increasing less than in ff. Among other HybNs, the number of PECs increases with the rise in the NPVF. HybNs with the highest increases in PEC are *PC*- and *PP*-shaped HybNs, with 2.27% and 3.24%, respectively. The difference in PEC numbers between PP- and *SS*-shaped HybNs with the highest and lowest PEC numbers, respectively, is about 20%. Note that the PEC number is higher in HybNs formed with *P*-shaped nanoparticles. At Re = 10,000, the PEC number is less than unity in all HybNs. This is because the ff ratio increases more than the heat transfer ratio.

In Fig. 10, it can be seen that the TEG changes at a constant Re of 10,000 for a 60%:40% SiO_2-MWCNT/water HybN with various nanoparticle shapes and NPVFs. In general, the graph shows that TEG decreases with increasing NPVF in all HybNs. The decreasing trend of each HybN differs from the others. For example, the change of TEG from HybNs with second nanoparticle shapes *S*, *C*, and *P* are *S*-, *C*-, and *P*-shaped HybNs in increasing order. This situation is because the heat conduction capacity of each nanoparticle with different shapes is different. In other words, the effect of each nanoparticle on heat transfer is different. This effect becomes essential with the increase in the NPVF. Considering HybNs with varying shapes of nanoparticle at a constant 1.0% NPVF, the TEG of *CS*-, *SS*-, *PC*-, *CC*-, *SC*-, *PP*-, *CP*-, and *SP*-shaped HybNs compared to *PS*-shaped HybNs is greater by 1.4%, 2.53%, 44.10%, 46.91, 48.87%, 58.98%, 62.07%, and 64.60%, respectively. As the NPVF and nanoparticle shape change, the velocity of the fluid changes. Changes in fluid velocity have significant effects on heat transfer. The slope of TEG is greater in HybNs with more outstanding heat transfer. Looking at the graph in light of this information, the *SP*-, *CP*-, and *PP*-shaped HybNs at the top perform more heat transfer, so their TEG slope is higher.

Figure 11 depicts the variation in FEG at a constant Re for a 60%:40% SiO_2-MWCNT/water HybN with various nanoparticle shapes and NPVFs (0.2%, 0.6%, 1.0%). Unlike the TEG change, with the increase in the NPVFs in the FEG graph, FEG increases in all HybNs depending on the nanoparticle shape. The *PP*-shaped HybN exhibits the highest growth with the rise of the NPVF, while the *SS*-shaped HybN exhibits an almost negligible change. With the increase in the NPVF, the FEG changes increased more in percentage. The reason for this can be explained as the increase in the viscosity of HybNs with the rise in the NPVF. HybNs with the first or second nanoparticle shape *P* have higher FEG values than other HybNs. For example, *SP*-, *SC*-, and *SS*-shaped HybNs have a FEG of 15.90% greater than that of *SS* at NPVF of 1.0%. When the FEG of *PS*-, *PC*-,

and *PP*-shaped HybNs is compared, the FEG value of *PP* is 17.82% higher than that of *PS*-shaped HybN.

Figure 12 shows the distributions in ff at a constant Re for a 60%:40% SiO_2-MWCNT/water HybN with various nanoparticle shapes and NPVFs (0.2%, 0.6%, 1.0%). Looking at the TTEG chart, it can be noticed that the same trend is present in the TEG chart. The reason behind this situation can be interpreted as the heat transfer effects of all the different nanoparticle-shaped hybrid nanofluids used in the study being more dominant than the viscous effects. Regarding entropy production, the best fluid is a *PS* nanoparticle-shaped HybN.

Figure 13 represents the variation in exergy destruction at a constant Re for a 60%:40% SiO_2-MWCNT/water HybN with various nanoparticle shapes and NPVFs (0.2%, 0.6%, 1.0%). When the graph is examined, the exergy destruction decreases with the increase of the NPVF. This situation can be interpreted as a decrease in exergy destruction due to the increase in thermal characteristics of all HybNs used in the study due to the increase in the NPVF. Exergy destruction value increases in HybNs with second nanoparticle shapes *S*, *C*, and *P*, respectively. For example, when *comparing PS-, PC-, and PP-shaped* HybN*s,* HybN*s with second nanoparticle shapes C and P* have 43.90% and 58.74% higher exergy destruction than *S*, respectively. In other words, the most dominant nanoparticle shape on exergy destruction is *P*. At the same time, the most ineffective is *S*. The most suitable HybN for use in terms of exergy destruction is the *PS* shape. In addition, the nanoparticle shape, not the NPVF of the HybN, has the greatest effect on exergy destruction change.

Figure 14 depicts the variation in exergy efficiency at a constant Re for a 60%:40% SiO_2-MWCNT/water HybN with various nanoparticle shapes and NPVFs (0.2%, 0.6%, 1.0%). The exergy efficiency graph shows the opposite variation of the exergy destruction distribution. As it is known, it is evident that the less exergy destruction, the higher the exergy efficiency will be. While the exergy efficiency of *PC*, *CC*-, *SC*-, *PP*-, *CP*-, and *SP*-shaped HybNs increases rapidly with the increase of NPVF, the effect on the exergy efficiency of *PS*-, *CS*-, and *SS*-shaped HybNs is almost negligible. According to the graph, the *PS*-shaped HybN exhibits the maximum exergy efficiency, while the *SP*-formed HybN shows the minimum exergy efficiency. This can be interpreted as *SP* having smaller TTEG and exergy destruction values, while *PS* has larger TTEG and exergy destruction values.

Figure 15 represents the temperature distribution at the exit of the channel at a constant Re of 10,000 in different nanoparticle shapes (SS, SC, SP, CS, CC, CP, PS, PC, and PP) and 0.6% NPVF of 60%:40% SiO_2-MWCNT/water HybN. Considering the temperature changes, the exit temperature is highest when the first nanoparticle is *S*, while the exit temperature is the lowest when the first nanoparticle is

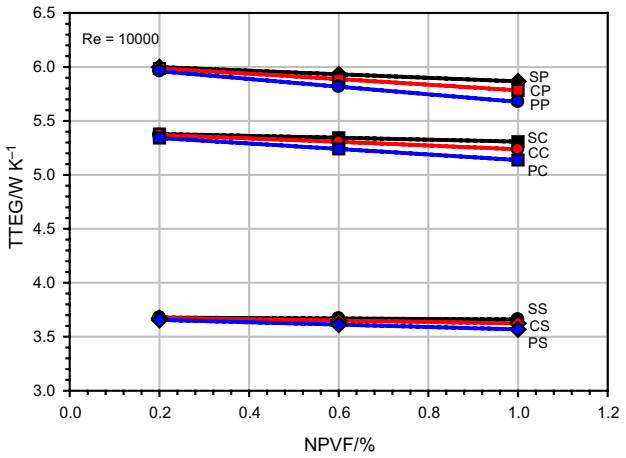

Fig. 12 Distributions of TTEG for different shapes of nanoparticles and NPVF

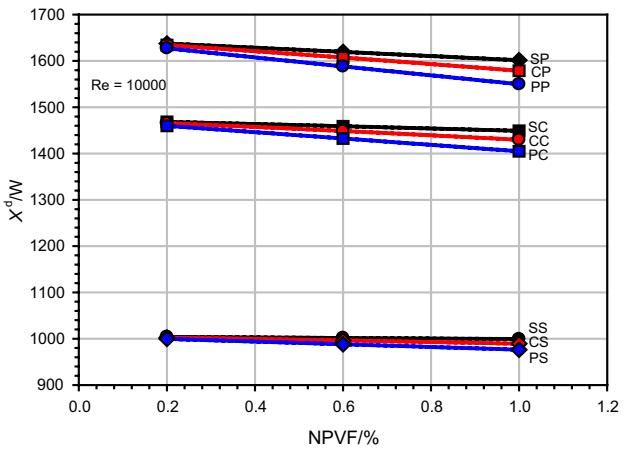

Fig. 13 Variations of exergy destruction for different shapes of nanoparticles and NPVF

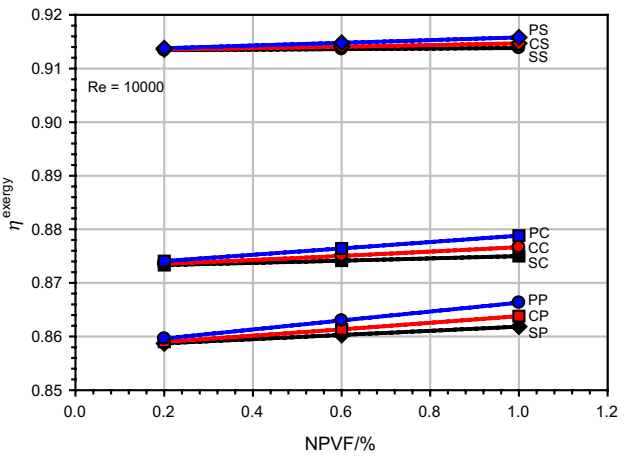

Fig. 14 Distributions of exergy efficiency for different shapes of nanoparticles and NPVF

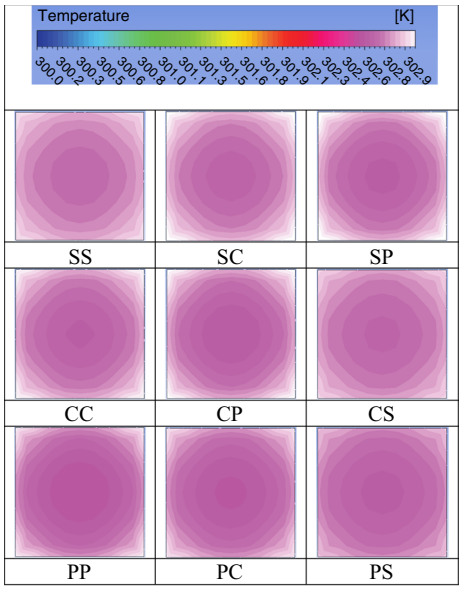

Fig. 15 Temperature contours for different shapes of nanoparticles at NPVF = 0.6% and Re = 10,000

P. When the first nanoparticle is *P*, the heat transfer coefficient will take the greatest value since the low exit temperature will decrease the bulk temperature (see Eq. 19).

Figure 16 presents velocity distribution at the exit of the channel at a constant Re of 10,000 in different nanoparticle shapes (*SS*, *SC*, *SP*, *CS*, *CC*, *CP*, *PS*, *PC*, *PP*) and 0.6% NPVF of 60%:40% SiO_2-MWCNT/water HybN. When the figures are examined, the velocity distribution of HybNs in which the first nanoparticle is *P* shows an increase toward the walls. As the velocity increases, the outlet temperature is lower, and the bulk temperature is also lower. As the bulk temperature is low, the heat transfer coefficient also increases, and as a result, the heat transfer increases.

Figure 17 represents the temperature distribution at the exit of the channel at a constant Re of 10,000 in different nanoparticle shapes and 1.0% NPVF of 60%:40% SiO_2-MWCNT/water HybN. When the graph is examined, the temperature distributions differ according to Fig. 15. With the NPVF being 1.0%, the colors showing the temperature changes become darker. In other words, the temperature values decreased more than in Fig. 15. As stated above, the bulk temperature decreases with decreasing outlet temperature. As a result, heat transfer increased by more than 0.6% NPVF.

Figure 18 shows the velocity distribution at the exit of the channel at a constant Re of 10,000 in different nanoparticle shapes and 1.0% NPVF of 60%:40% SiO_2-MWCNT/water HybN. When the figure is examined, velocity changes increased more in all nanoparticle shapes than in Fig. 16. This confirms that the increase in the NPVF increases the heat transfer due to the increase in the velocity.

Effect of Re on the nanoparticle shape of the HybN

Figure 19 shows the variation of the Nu of the 60%:40% SiO_2-MWCNT/water HybN with different nanoparticle shapes for various Res. As can be seen from the graph, HybNs with water and different nanoparticle shapes increase the Nu with increasing Re. When the Nu of HybNs is compared with water, at some Res, water is higher than that of HybNs. For example, *SS*, *SC*-, *SP*-, *CC*-, *CP*-, *PP*-, and *PC*-shaped HybNs increase the Nu more than water at Res

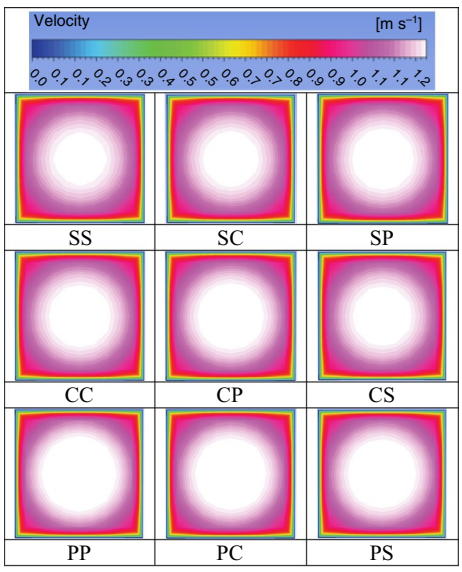

Fig. 16 Velocity contours for different shapes of nanoparticles at NPVF = 0.6% and Re = 10,000

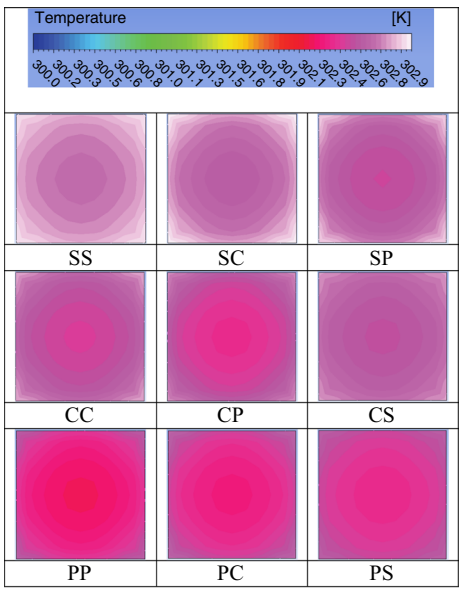

Fig. 17 Temperature contours for different shapes of nanoparticles at NPVF = 1.0% and Re = 10,000

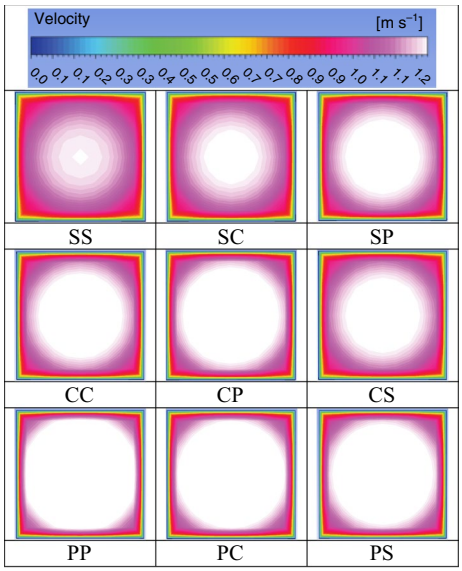

Fig. 18 Velocity contours for different shapes of nanoparticles at NPVF = 1.0% and Re = 10,000

of 3000, 4000, and 5000, while CS- and PS-shaped HybNs are lower. When the Re is 6000, *SS*-, *CS*-, and *PS*-shaped nanofluids decreased the Nu compared to water. However, at Res of 9000 and 10,000, the Nu of water is higher than all HybNs. When evaluated in terms of Nu, Res of 9000 and 10,000 values should not be used for HybNs.

Figure 20 presents the changing of the ff of the 60%:40% SiO_2-MWCNT/water HybN with different nanoparticle shapes for various Res. When the graph is first looked at, the ff decreases with the increase of the Re. As expected, the ff of HybNs obtained by adding nanoparticles to water is higher than water due to the increase in viscosity. It is determined that the ff decreased rapidly in the first Res used in the study. Then, it is seen that the ff decrease rate slows down. At Re of 3000, HybNs with *SP* and *CS* nanoparticle shapes have the closest values to the ff of water with 0.07% and 1.35%, respectively. Res, *CP*-, and *PP*-shaped HybNs exhibit the highest friction factors among all fluids.

Figure 21 represents the variation of the PEC number of the 60%:40% SiO_2-MWCNT/water HybN with different nanoparticle shapes for various Res. The PEC number is an essential parameter in heat transfer applications. If the PEC number is greater than unity, it is understood that the heat transfer mechanism is dominant, and if it is less than unity, the friction mechanism is more dominant. The graph compares the number of PECs with that of water. For this reason, if the PEC number is greater than unity, it can be interpreted as a better performance than water, and if it is less than unity, it can be construed as a worse performance. Looking at the graph, with the increase of the Re, the PEC number decreases in the fluids used in the whole system and falls below unity. This means that using hybrid nanofluids for this system at high Res decreased performance compared to water. HybNs with *SP* and *PP* nanoparticle shapes show the highest PEC number at Re of 3000, while HybNs with *SS* shapes show the lowest PEC number at Re of 10,000. *SP*, *CP*, and *PP* nanoparticle-shaped HybNs perform better than water with Re up to 7000; *SC*, *CC*, and *PC* nanoparticle-shaped HybNs up to 6000; *SS*, *CS*, and *PS* nanoparticle-shaped HybNs with Re up to 5000. In other words, HybNs with the second particle shape *P* can be interpreted as providing better performance at higher Res.

Figure 22 shows the variation of the TEG of the 60%:40% SiO_2-MWCNT/water HybN with different nanoparticle shapes for various Res. Looking at the graph, TEG decreases

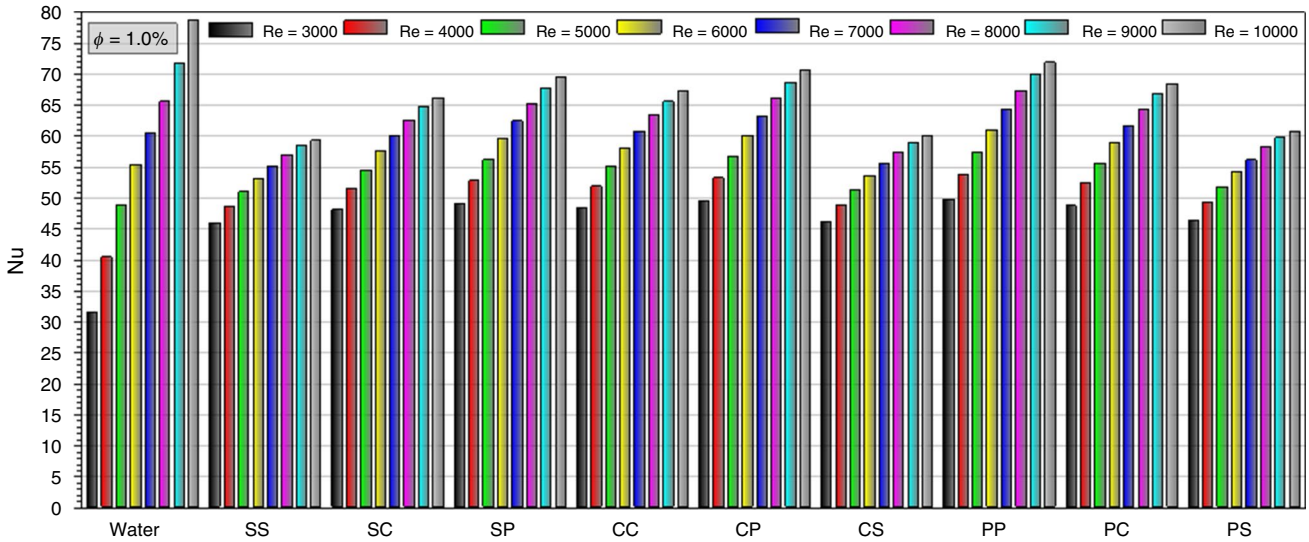

Fig. 19 Distributions of Nu for different shapes of nanoparticles and Res

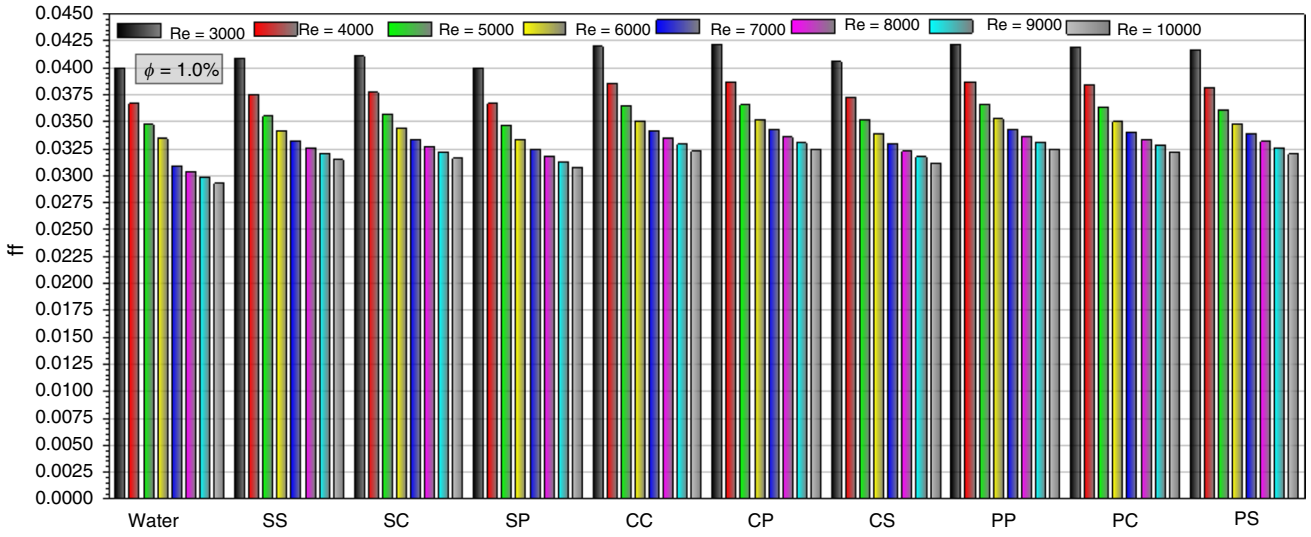

Fig. 20 Variations of ff for different shapes of nanoparticles and Res

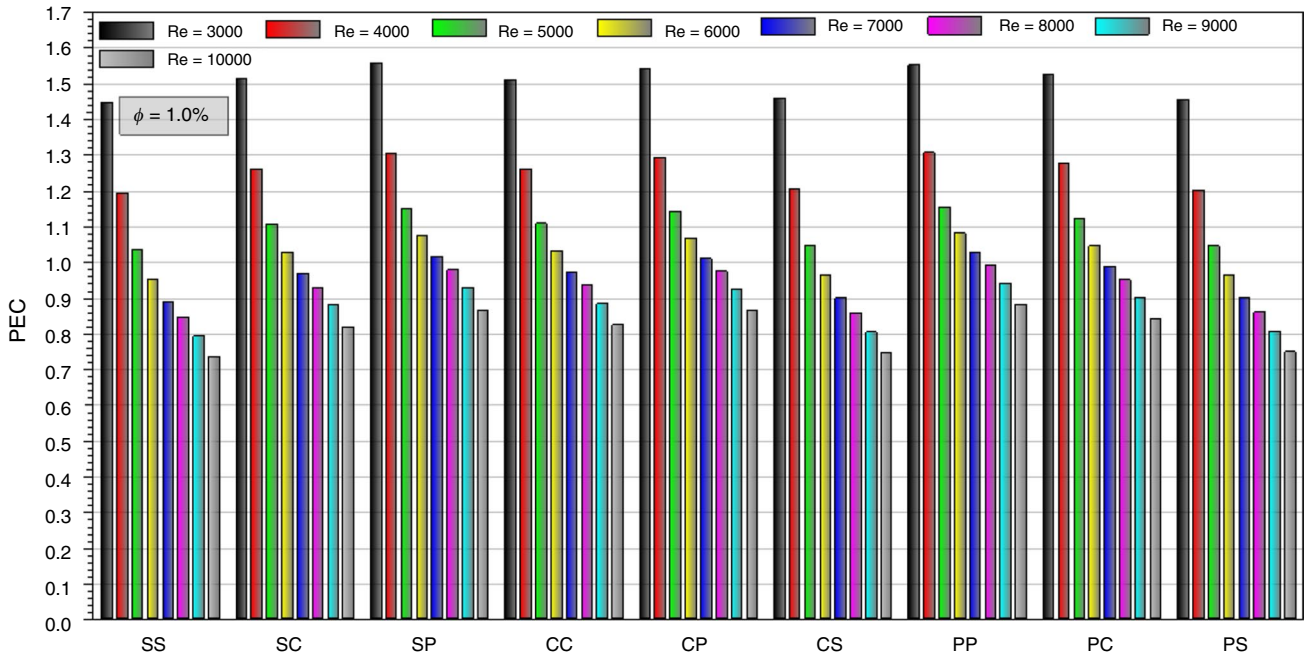

Fig. 21 Distributions of PEC for different shapes of nanoparticles and Res

with an increasing Re in all working fluids. This can be interpreted as the increase in the Nu due to the increase in the heat transfer coefficient with the increase of the Re. With the increase in Re, the decreasing trend of *SS*-, *CS*-, and *PS*-shaped HybNs is less than that of other HybNs with different nanoparticle shapes. The reason for this can be interpreted as HybNs with *SS*, *CS*, and *PS* nanoparticle shapes increase heat transfer less than other HybNs.

Figure 23 shows the interpretation of the FEG of the 60%:40% SiO_2-MWCNT/water HybN with varying forms of nanoparticle for various Res. As can be seen from the graph, FEG increases with increasing Re. This is because

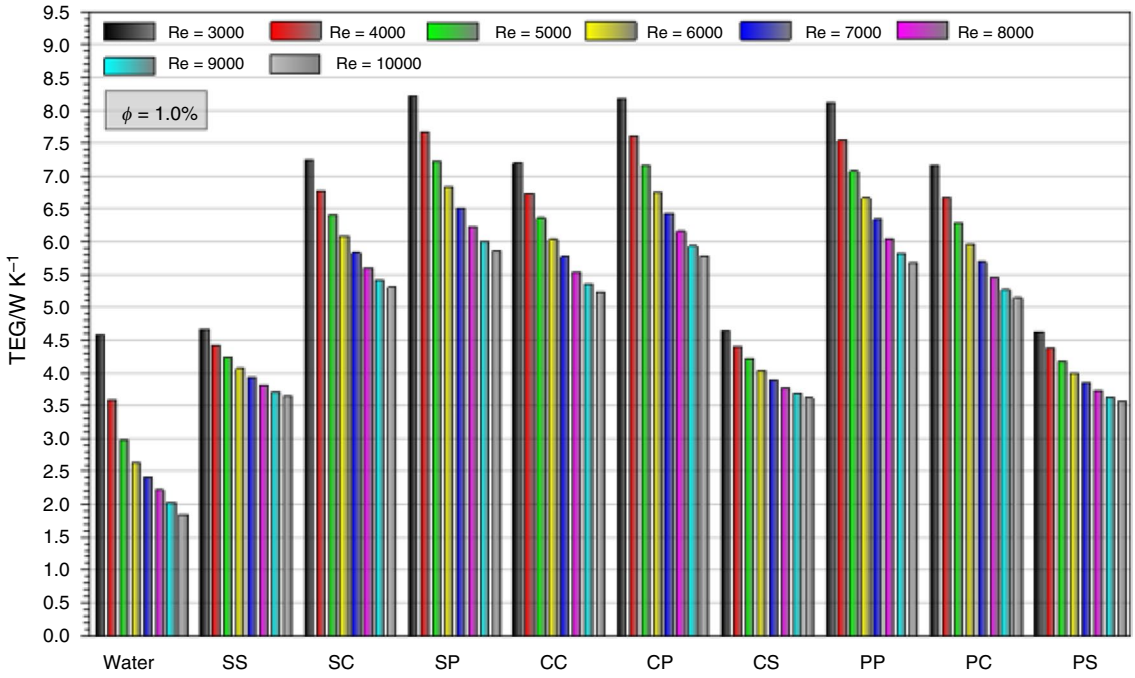

Fig. 22 Distributions of TEG for different shapes of nanoparticles and Res

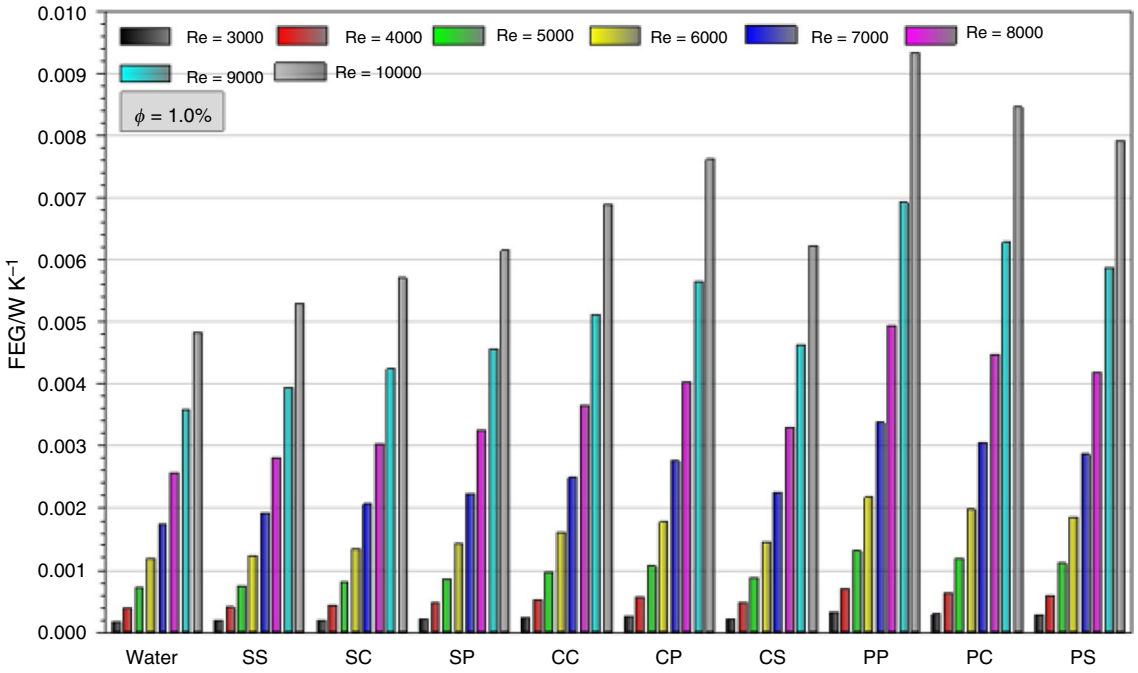

Fig. 23 Variations of FEG for different shapes of nanoparticles and Res

the pressure drop increases with rising Re. The *PP*-shaped HybN shows the highest FEG.

Figure 24 shows the variation of the TTEG of the 60%:40% SiO_2-MWCNT/water HybN with different

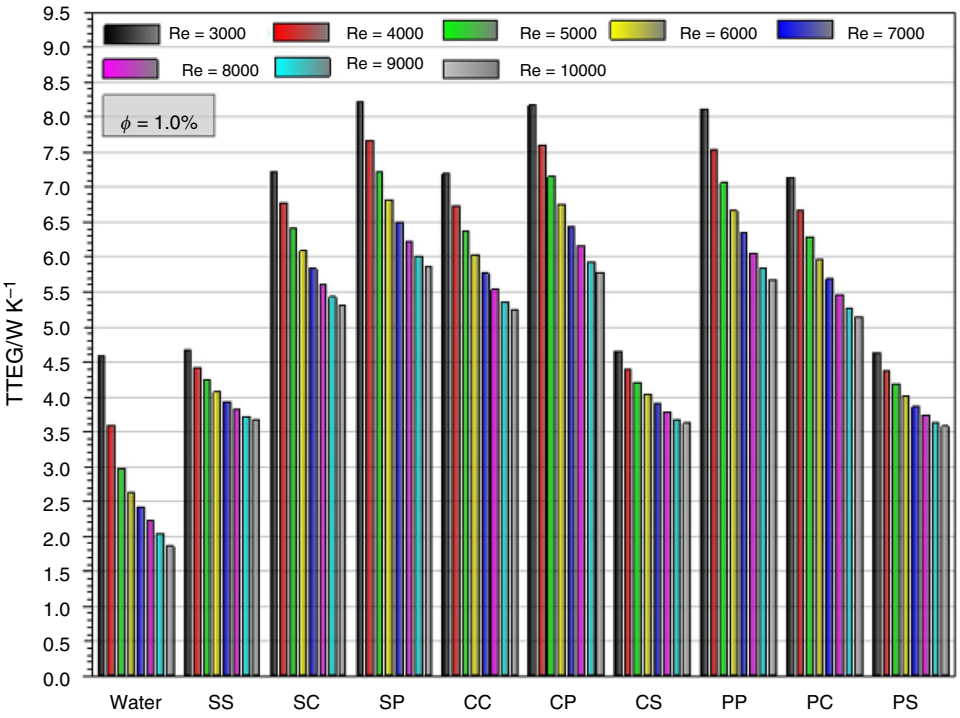

Fig. 24 Distributions of TTEG for different shapes of nanoparticles and Res

nanoparticle shapes for various Res. If the figure is examined, it can be seen that it has the same trend as the TEG graph, as the entropy generation from heat transfer is more dominant. With the increase of Re, the minor effect on TEG occurs in the *CS*-shaped HybN, while the greatest impact occurs in the *SP*-shaped HybN.

Figure 25 shows the variation of the exergy destruction of the 60%:40% SiO_2-MWCNT/water HybN with

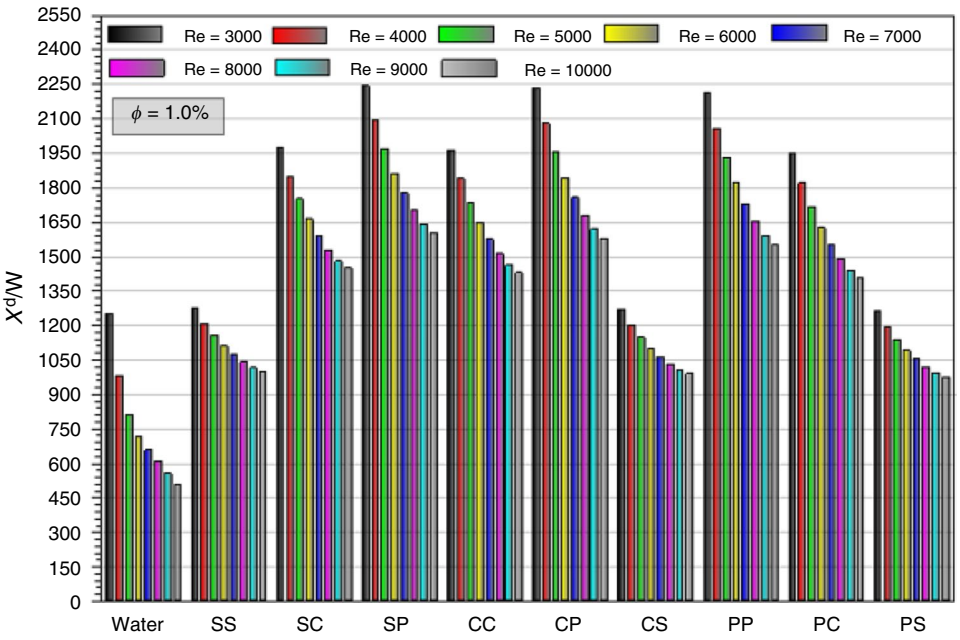

Fig. 25 Variations of exergy destruction for different shapes of nanoparticles and Res

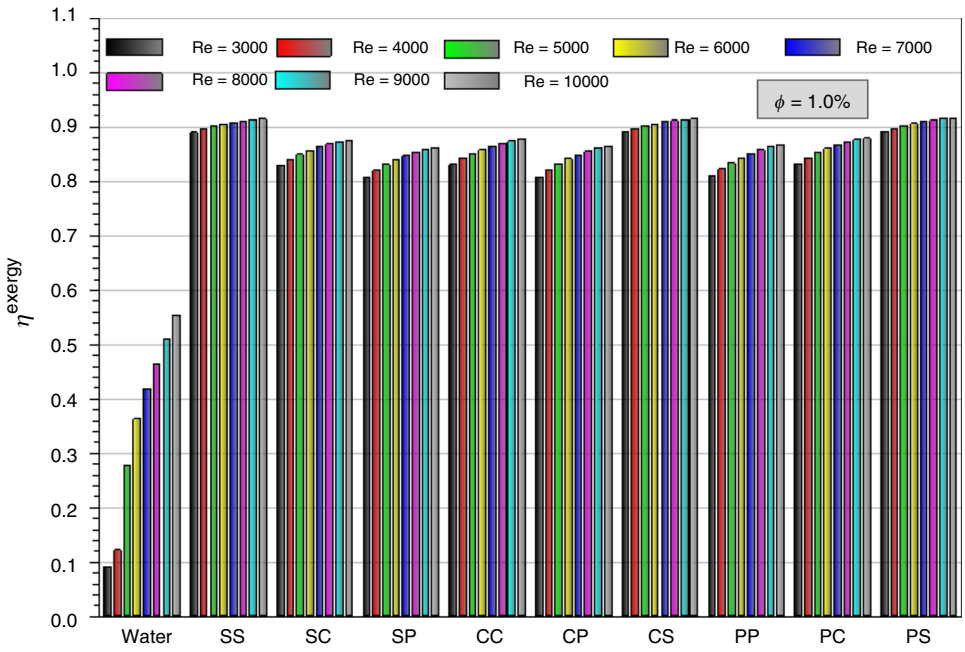

Fig. 26 Distributions of exergy efficiency for different shapes of nanoparticles and Res

different nanoparticle shapes for various Res. Looking at the graph, the Re greatly influences the exergy destruction change. At Re of 3000, exergy destruction reaches approximately 2250 W at the highest and 1300 W at the lowest. Exergy destruction decreases from all HybNs with increasing Re. An increase in the Re causes an increase in the velocity of the fluid, as a result of which the temperature change decreases. The decrease in temperature change causes the bulk temperature to decrease. As a result, the heat transfer increases with an increase in the Re. Exergy destruction decreases with the increase in heat transfer.

Figure 26 shows the variation of the exergy efficiency of the 60%:40% SiO_2-MWCNT/water HybN with different nanoparticle shapes for various Res. When the graph is examined, it can be said that all HybNs are more suitable for the system regarding exergy efficiency than water. The higher the Re, the higher the exergy efficiency. While the effect on the exergy efficiency with the change of Re is on the water the most, the impact on the HybNs with different nanoparticle shapes used in the system is less. In other words, with the increase of Re, the exergy efficiency of water increases more in percent, while the efficiency increases less in HybNs.

Figure 27 exhibits the variation of the temperature contours of the 60%:40% SiO_2-MWCNT/water HybN with different nanoparticle shapes for Res of 3000 and 6000. According to the graph, with the increase of the Re, there is a decrease in the exit temperature due to the increase in velocity. With the rise of the Re, the temperature decreases of the HybNs with the first nanoparticle shape *P* were higher than the other HybNs. In addition, the temperature distribution of these HybNs shows a more uniform distribution.

Figure 28 shows the variation of the temperature contours of the 60%:40% SiO_2-MWCNT/water HybN with different nanoparticle shapes for Res of 3000, 6000, and 10,000. Looking at the graph, it is seen that the velocity distribution changes significantly with the increase of the Re. In HybNs with the first nanoparticle shape *P*, it is seen that the flow velocity is higher at the walls of the channel with the increase of the Re. In this case, distortions occur in the thermal boundary layer, and this causes a further increase in heat transfer.

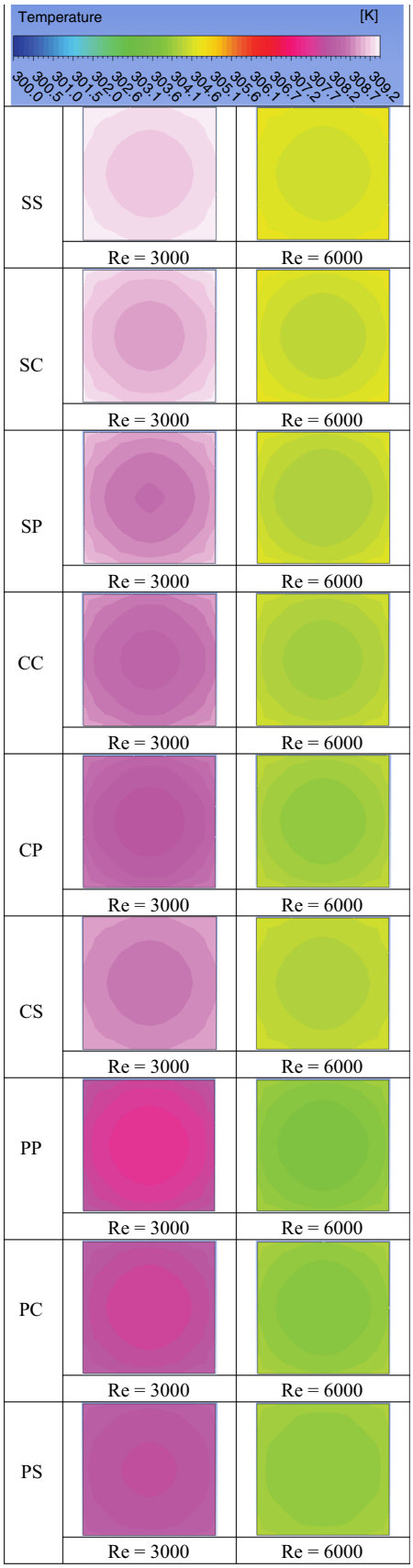

Fig. 27 Temperature contours for different shapes of nanoparticles at NPVF = 1.0% and different Res

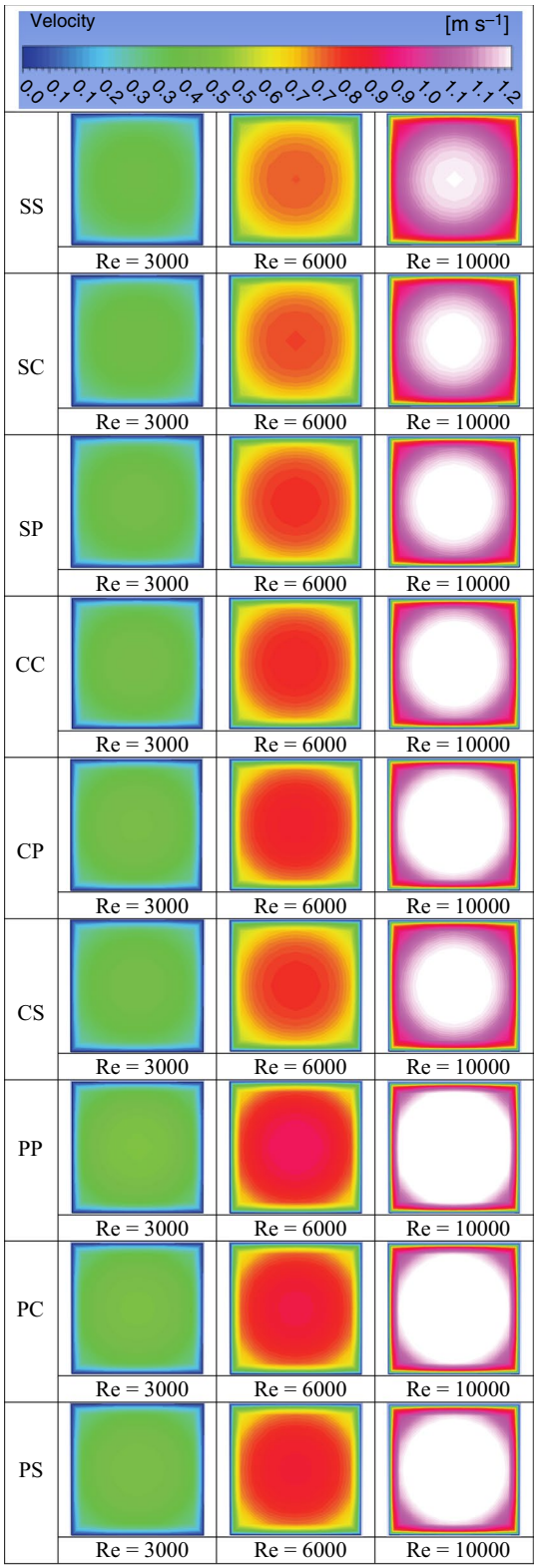

Fig. 28 Velocity contours for different shapes of nanoparticles at NPVF = 1.0% and different Res

Conclusions

This research analyzes the heat and flow characteristics of a 60%:40% SiO2-MWCNT/water HybN with a variety of nanoparticle shapes at a range of NPVFs and Res in a 3D square duct using a two-phase flow technique. The Nu, ff, PEC, TEG, FEG, TTEG, exergy destruction and efficiency, temperature, and velocity contours are given in detail for the stated parameters above.

The most important findings from this paper are briefly discussed below.

- Modifying the nanoparticle's form has a greater impact on the Nu than changing the NPVF.
- While the pressure losses are greatest in the *P*-shaped nanoparticle-containing HybN, the *S*-shaped nanoparticle-containing HybN has the lowest pressure losses.
- As the volume percentage of nanoparticles is 1.0%, the ff is increased by 5.54% in the *PP*-shaped HybN compared to the *SP*-shaped HybN.
- The TEG of *CS*-, *SS*-, *PC*-, *CC*-, *SC*-, *PP*-, *CP*-, and *SP*-shaped HybNs is higher than *PS*-shaped HybNs by 1.4%, 2.53%, 44.10%, 46.91%, 48.87%, 62.07%, and 64.60%, respectively, when the NPVF and Re are held constant at 1.0% and 10,000, respectively.
- In comparing *PS*-, *PC*-, and *PP*-shaped HybNs, the exergy destruction of the HybNs with the second nanoparticle forms *C* and *P* is 43.90% and 58.74% greater, respectively.
- Better performance at higher Res may be interpreted for *hybrid nanofluid*s with the second particle shape of *P*.
- It may be concluded that all HybNs are more exergy-efficient for the system than water.

Recommendations for future studies

As this research is a recent addition to the existing literature, future studies may investigate other factors within this study. Here are a few examples:

- The investigation may be conducted under circumstances of transient and laminar flow.
- The investigation may be experimentally conducted, and its results can be compared with a machine learning approach.
- Different types of ternary and tetra HybNs can be used to investigate the effects of nanoparticle shapes regarding heat and flow features.

Funding Open access funding provided by the Scientific and Technological Research Council of Türkiye (TÜBİTAK).

References

1. Hu H, Wang H, Zou Z, Zhu J. Investigation of inter-zonal heat transfer in large space buildings based on similarity: comparison of two stratified air-conditioning systems. Energy Build. 2022;254:111602.
2. Reddy YD, Goud BS, Chamkha AJ, Kumar MA. Influence of radiation and viscous dissipation on MHD heat transfer Casson nanofluid flow along a nonlinear stretching surface with chemical reaction. Heat Transf. 2022. https://doi.org/10.1002/htj.22460.
3. Deb S, Kanade PM, Pal S, Das AK. Influence of horizontal enhanced tube on flow boiling heat transfer characteristics of environmentally friendly refrigerant R-407c. Mater Today Proc. 2022;62:3178–82.
4. Liu B, Lu M, Shui B, Sun Y, Wei W. Thermal-hydraulic performance analysis of printed circuit heat exchanger precooler in the Brayton cycle for supercritical CO2 waste heat recovery. Appl Energy. 2022;305:117923.
5. Huang J, Wang C, Guo K, Zhang D, Su GH, Tian W, et al. Heat transfer analysis of heat pipe cooled device with thermoelectric generator for nuclear power application. Nucl Eng Des. 2022;390:111652.
6. Ahmed S, Li S, Li Z, Xiao G, Ma T. Enhanced radiative cooling of solar cells by integration with heat pipe. Appl Energy. 2022;308:118363.
7. Alrashidi A. Numerical study of conjugate heat transfer for cooling the circuit board. J Electron Cool Therm Control. 2016;06:120.
8. Ganvir RB, Walke PV, Kriplani VM. Heat transfer characteristics in nanofluid—a review. Renew Sustain Energy Rev. 2017;75:451–60.
9. Suleimanov BA, Ismailov FS, Veliyev EF. Nanofluid for enhanced oil recovery. J Pet Sci Eng. 2011;78:431–7.
10. Gülmüş B, Muratçobanoğlu B, Mandev E, Afshari F. Experimental and numerical investigation of flow and thermal characteristics of aluminum block exchanger using surface-modified and recycled nanofluids. Int J Numer Methods Heat Fluid Flow. 2023;33:2685–709.
11. Xuan Y, Li Q. Heat transfer enhancement of nanofluids. Int J Heat Fluid Flow. 2000;21:58–64.
12. Yu W, Xie H, Chen L, Li Y. Enhancement of thermal conductivity of kerosene-based Fe_3O_4 nanofluids prepared via phase-transfer method. Colloids Surf Physicochem Eng Asp. 2010;355:109–13.
13. Lau GE, Mohammadpour J, Lee A. Cooling performance of an impinging synthetic jet in a microchannel with nanofluids: an Eulerian approach. Appl Therm Eng. 2021;188:116624.
14. Davarnejad R, Jamshidzadeh M. CFD modeling of heat transfer performance of MgO-water nanofluid under turbulent flow. Eng Sci Technol Int J. 2015;18:536–42.

15. Subramanian R, Rengasamy S, Sakthi A. Maternal risk factors for low birth weight in neonates—a community-based prospective study in rural area of Puducherry. Int J Med Sci Public Health. 2019;1:386–91.
16. Mahato SK, Rana SC, Barman RN. Effect of Al_2O_3/Water and CuO/water nanofluids on heat transfer enhancement flows through twisted clockwise–counter-clockwise square duct. Arab J Sci Eng. 2022;47:8141–59.
17. Heidary H, Kermani MJ. Effect of nano-particles on forced convection in sinusoidal-wall channel. Int Commun Heat Mass Transf. 2010;37:1520–7.
18. Liu F, Cai Y, Wang L, Zhao J. Effects of nanoparticle shapes on laminar forced convective heat transfer in curved ducts using two-phase model. Int J Heat Mass Transf. 2018;116:292–305.
19. Zeinali Heris S, Nassan TH, Noie SH, Sardarabadi H, Sardarabadi M. Laminar convective heat transfer of Al_2O_3/water nanofluid through square cross-sectional duct. Int J Heat Fluid Flow. 2013;44:375–82.
20. Bhattad A, Sarkar J, Ghosh P. Hydrothermal performance of different alumina hybrid nanofluid types in plate heat exchanger. J Therm Anal Calorim. 2020;139:3777–87.
21. Zufar M, Gunnasegaran P, Ng KC, Mehta HB. Evaluation of the thermal performance of hybrid nanofluids in pulsating heat pipe. CFD Lett. 2019;11:13–24.
22. Bahiraei M, Mazaheri N, Aliee F. Second law analysis of a hybrid nanofluid in tubes equipped with double twisted tape inserts. Powder Technol. 2019;345:692–703.
23. Ferrouillat S, Bontemps A, Ribeiro J-P, Gruss J-A, Soriano O. Hydraulic and heat transfer study of SiO_2/water nanofluids in horizontal tubes with imposed wall temperature boundary conditions. Int J Heat Fluid Flow. 2011;32:424–39.
24. Khan WA, Khan ZH, Rahi M. Fluid flow and heat transfer of carbon nanotubes along a flat plate with Navier slip boundary. Appl Nanosci. 2014;4:633–41.
25. Khairul MA, Alim MA, Mahbubul IM, Saidur R, Hepbasli A, Hossain A. Heat transfer performance and exergy analyses of a corrugated plate heat exchanger using metal oxide nanofluids. Int Commun Heat Mass Transf. 2014;50:8–14.
26. Fadodun OG, Kaood A, Hassan MA. Investigation of the entropy production rate of ferrosoferric oxide/water nanofluid in outward corrugated pipes using a two-phase mixture model. Int J Thermal Sci. 2022;178:107598.
27. Manninen M, Taivassalo V, Kallio S. On the mixture model for multiphase flow. Vtt Publ. 1996;1–67.
28. Schiller L. A drag coefficient correlation. Zeit Ver Deutsch Ing. 1933;318–20.
29. Bengt SMR. Turbulence modeling experience in ducts with forced convection flow. Numer Heat Transf Part Appl. 1999;35:629–54.
30. ANSYS Fluent Theory Guide. Lebanon. New Hampshire: Fluent Corporation; 2006.
31. Newton R. Advantages of SiO_2. Los Angeles: University of California; 1996.
32. Arabpour A, Karimipour A, Toghraie D. The study of heat transfer and laminar flow of kerosene/multi-walled carbon nanotubes (MWCNTs) nanofluid in the microchannel heat sink with slip boundary condition. J Therm Anal Calorim. 2018;131:1553–66.
33. Moghadassi A, Ghomi E, Parvizian F. A numerical study of water based Al_2O_3 and Al_2O_3–Cu hybrid nanofluid effect on forced convective heat transfer. Int J Therm Sci. 2015;92:50–7.
34. Sahu M, Sarkar J. Steady-state energetic and exergetic performances of single-phase natural circulation loop with hybrid nanofluids. J Heat Transf. 2019. https://doi.org/10.1115/1.4043819.
35. Maxwell: A treatise on electricity and magnetism. Oxford: Clarendon Press; 1873
36. Manca O, Nardini S, Ricci D. A numerical study of nanofluid forced convection in ribbed channels. Appl Therm Eng. 2012;37:280–92.
37. Shahsavar A, Rashidi M, Mosghani MM, Toghraie D, Talebizadehsardari P. A numerical investigation on the influence of nanoadditive shape on the natural convection and entropy generation inside a rectangle-shaped finned concentric annulus filled with boehmite alumina nanofluid using two-phase mixture model. J Therm Anal Calorim. 2020;141(2):915–30.
38. Bahiraei M, Mazaheri N, Moayedi H. Employing V-shaped ribs and nanofluid as two passive methods to improve second law characteristics of flow within a square channel: a two-phase approach. Int J Heat Mass Transf. 2020;151:119419.
39. Dittus FW. BLMK. Heat transfer in automobile radiators of tubular type. Berkeley: University of California Press; 1930.
40. Petukhov BS. Heat Transfer and Friction in Turbulent Pipe Flow with Variable Physical Properties. Adv Heat Transf. 1970;6:503–64.
41. Blasius P.R.H. Das Aehnlichkeitsgesetz bei Reibungsvorgangen in Flüssigkeiten. Forschungsheft; 1913.